

Model of Radiation and Heat Transfer in Laser-Powder Interaction Zone at Selective Laser Melting

A. V. Gusarov

I. Yadroitsev

Ph. Bertrand

I. Smurov

DIPI Laboratory,
Ecole Nationale d'Ingénieurs de Saint-Etienne
(ENISE),
58 rue Jean Parot,
Saint-Etienne 42023, France

A model for coupled radiation transfer and thermal diffusion is proposed, which provides a local temperature field. Single-line scanning of a laser beam over a thin layer of metallic powder placed on a dense substrate of the same material is studied. Both the laser beam diameter and the layer thickness are about 50 μm . The typical scanning velocity is in the range of 10–20 cm/s. An effective volumetric heat source is estimated from laser radiation scattering and absorption in a powder layer. A strong difference in thermal conductivity between the powder bed and dense material is taken into account. The above conditions correspond to the technology of selective laser melting that is applied to build objects of complicated shape from metallic powder. Complete remelting of the powder in the scanned zone and its good adhesion to the substrate ensure fabrication of functional parts with mechanical properties close to the ones of the wrought material. Experiments with single-line melting indicate that an interval of scanning velocities exists, where the remelted tracks are uniform. The tracks become “broken” if the scanning velocity is outside this interval. This is extremely undesirable and referred to as the “balling” effect. The size and the shape of the melt pool and the surface of the metallurgical contact of the remelted material to the substrate are analyzed in relation to the scanning velocity. The modeling results are compared with experimental observation of laser tracks. The experimentally found balling effect at scanning velocities above ~ 20 cm/s can be explained by the Plateau-Rayleigh capillary instability of the melt pool. Two factors destabilize the process with increasing the scanning velocity: increasing the length-to-width ratio of the melt pool and decreasing the width of its contact with the substrate. [DOI: 10.1115/1.3109245]

Keywords: powder bed, absorbing scattering medium, melt pool, capillary instability

1 Introduction

The process of selective laser melting (SLM) is a technique of direct manufacturing from metallic powder. Its principal difference from conventional powder metallurgy processes is local heating and binding of powder by a scanning laser beam. Rapid manufacturing [1] of complex parts (see examples in Fig. 1(a)) is assured by this method. The SLM includes scattering and absorption of laser radiation in the powder, heat conduction, melting and coalescence of powder particles, formation of the melt pool, and its solidification. Figure 1(b) shows a typical scheme of layer-by-layer SLM fabrication. A SLM machine comprises of a fabrication plate (1) with two holes to which two containers are attached. A roller (2) delivers powder from the left container and deposits a thin powder layer in the right container (I). The thickness of the layer (about 50 μm [2]) is controlled by pistons moving up (3) and down (4). The deposited layer is scanned by a laser beam (5), which ensures local melting and binding to the previously fabricated layer (II). A part of a complex shape can be obtained in the right container after multiple deposition-scanning cycles (III). The complete remelting of the powder in the scanning zone is shown in Fig. 1(c), and its good adhesion to the substrate ensures obtaining functional parts with high mechanical properties [2,3]. The

process of SLM is sensitive to a number of parameters such as the powder layer thickness, the power and the diameter of the laser beam, and the scanning speed.

Numerical simulation of heat transfer in the laser-powder interaction zone is applied to optimize the process parameters [4–9]. The thermal model by Bugeda et al. [5] simulates a laser beam moving along a straight line over the surface of a semi-infinite powder bed. The initial state of the material is uniform loose powder. Laser heating provokes coalescence of powder particles, which changes the effective thermal conductivity. Therefore, the equation of thermal diffusion is coupled with an equation of powder consolidation kinetics. The mechanism of consolidation by viscous flow driven by surface tension is studied in Ref. [5]. An Arrhenius-type dependence of viscosity versus temperature is employed, which can be applied to amorphous polymer powders. An improved kinetic equation is developed in Ref. [6] for crystalline polymers. A similar model of thermal diffusion coupled with consolidation kinetics proposed by Tolochko et al. [7] is adapted for metallic powders and takes into account the solid-state sintering controlled by diffusion below the melting point and instantaneous consolidation at melting. The above models neglect mass flow due to shrinkage at powder consolidation. A numerical approach to take the shrinkage into account is proposed in Ref. [8]. However, the shrinkage produces a nonflat top surface of the melt pool and provokes significant surface tension forces, whose influence on the free surface has not been rigorously calculated.

Models in Refs. [9–11] concern not only the laser-powder interaction zone but also the temperature distribution in the whole powder bed scanned by laser, which can be useful to calculate

Contributed by the Heat Transfer Division of ASME for publication in the JOURNAL OF HEAT TRANSFER. Manuscript received April 15, 2008; final manuscript received January 28, 2009; published online May 1, 2009. Review conducted by Ben Q. Li.

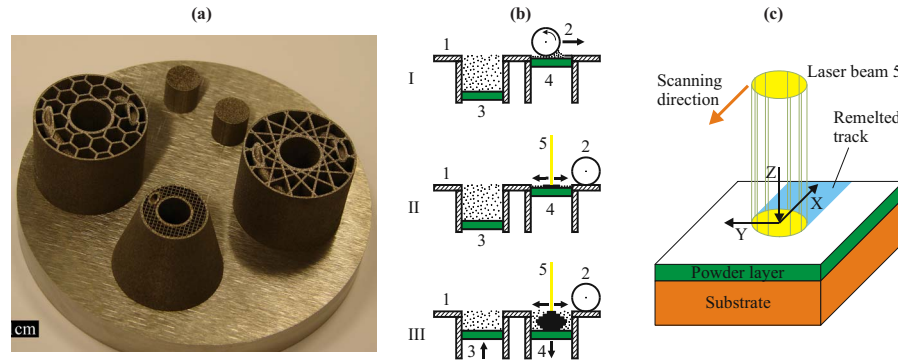


Fig. 1 Selective laser melting. (a) Fabricated parts. (b) Scheme of the process: (I) deposition of a powder layer, (II) scanning of the first layer, and (III) layer-by-layer fabrication. and (c) Detailed view of the laser-powder interaction zone: (1) fabrication plate, (2) roller, (3) powder delivery piston, (4) fabrication piston, and (5) laser beam.

residual thermal stresses [9]. Several consecutive laser scans along parallel lines on the surface of a semi-infinite powder bed are simulated. Such complicated geometry necessitates increased spatial resolution in calculations, and so these models are simplified relative to the detailed models of the interaction zone [5–8]. Thus, consolidation kinetics is simplified in Refs. [9–11], and models in Refs. [9,10] apply to the top powder layer and are essentially two dimensional.

The half-infinite powder bed was the target in the models of the interaction zone [5–7], while the complex target consisting of a powder layer on the top of a half-infinite solid was studied in recent works [8,12]. In the layer-by-layer technology, the solid substrate originates from the previously bound powder layers. Its thermal influence can be significant because of much higher thermal conductivity. In addition, this approach allows to consider the principal question about the binding between layers.

The conventional scheme where the laser beam directly strikes a continuous melt pool and the moving pool absorbs the loose powder is used in the model in Ref. [8], while the laser beam directly interacts with powder in the model in Ref. [12]. These two approaches can be distinguished as the model of immediate consolidation of powder after melting [8] and the model of slow consolidation [12]. The first approach is well known and approved, for example, at laser cladding. However, the hypothesis of immediate consolidation is not evident at SLM because the process parameters are considerably different, for example, the laser beam is one to two orders of magnitude thinner. Indeed, the experimentally measured time of coalescence of two 100–150 μm particles was in the range from several milliseconds to several tens of milliseconds [13], while the time of laser beam passage is of the order of a fraction of millisecond in the SLM machine [3]. Another reason to apply the model of slow consolidation, where the processes of radiation transfer and shrinkage are essentially separated in space is the experimentally observed detachment of the remelted material from the loose powder [3] (see also the discussion in Sec. 4).

This work concerns modeling the laser-powder interaction zone based on the assumption of slow consolidation and aims to clarify physical processes at SLM. A single-line scan on a layer of unconsolidated powder is studied, as shown in Fig. 1(c). The substrate is implied to be solid and thermally thick. The model includes laser radiation transfer described in Sec. 2 and conductive heat transfer described in Sec. 3.

2 Radiation Transfer

The freshly deposited powder is not mechanically compressed in the SLM machine in order to not destroy the underlying consolidated part. Therefore, it has as high porosity as freely poured powder, which is in the range 40–60% for typical metallic pow-

ders employed in SLM [14]. Laser radiation penetrates into powder through pores to a depth of several particle diameters because of multiple reflections [15]. This is comparable with the powder layer thickness. Thus, laser energy is deposited not on the surface but in the bulk of the powder layer. The objective of this section is to estimate the parameters of the volumetric heat source due to laser radiation absorption, which is necessary for further heat transfer calculations.

Figure 2 shows the model of radiation transfer, where the powder layer of thickness L is uniformly irradiated at normal incidence with power density Q_0 . The collimated incident beam is scattered inside the powder and gives rise to radiation propagating in all directions, which is characterized by its angular intensity $I(z, \theta)$ at depth z and polar angle θ . The radiation intensity is defined in the ordinary way as the energy flux through the unit surface of the plane parallel to the substrate at depth z (see Fig. 2) transferred by rays within a small solid angle about direction θ divided by this solid angle and by $\cos \theta$ [16]. Assuming a large area being irradiated that contains a great number of structural features, powder can be considered as a homogeneous absorbing scattering medium, and the radiation transfer equation (RTE) can be employed [17] as

$$\mu \frac{\partial I(z, \mu)}{\partial z} = \beta \left\{ \frac{\omega}{2} \int_{-1}^1 I(z, \mu') P(\mu', \mu) d\mu' - I(z, \mu) \right\} \quad (1)$$

where $\mu = \cos \theta$, β is the extinction coefficient, ω is the scattering albedo, and $P(\mu', \mu)$ is the scattering phase function. In the case of opaque powder particles, the effective values of the extinction coefficient and albedo are [17]

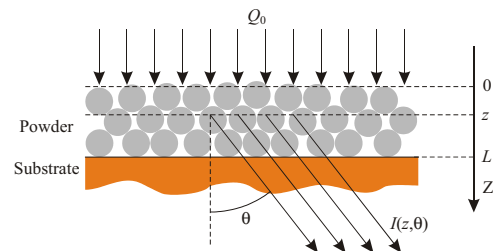


Fig. 2 Laser radiation transfer in a powder layer on a substrate: (Q_0) incident power density, (z) depth, (L) layer thickness, (θ) radiation propagation angle, and ($I(z, \theta)$) radiation intensity

$$\beta = S/4 \text{ and } \omega = \rho \quad (2)$$

where S is the specific powder surface per unit pore volume, and ρ is the hemispherical reflectivity of the powder material in the dense form. The scattering phase function can be obtained from the directional reflectivity of the powder material [17]. In the case of spherical metallic particles, the specular reflection law with constant directional reflectivity can be applied [16,17], which gives isotropic scattering

$$P(\mu', \mu) = 1 \quad (3)$$

The boundary condition on the powder surface $z=0$ specifies normally-collimated incident radiation

$$I(0, \mu) = \frac{Q_0}{2\pi} \delta(\mu - 1) \text{ at } \mu > 0 \quad (4)$$

where δ is the Dirac delta function. The specular reflection with reflectivity ρ is assumed on substrate surface $z=L$ as

$$I(L, \mu) = \rho I(L, -\mu) \text{ at } \mu < 0 \quad (5)$$

The radiation intensity I splits into two collimated terms and a diffused one [17]:

$$I(z, \mu) = \frac{Q_+(z)}{2\pi} \delta(\mu - 1) + \frac{Q_-(z)}{2\pi} \delta(\mu + 1) + F(z, \mu) \quad (6)$$

where Q_+ and Q_- are the power densities of the forward and backward, respectively. Collimated radiation originated from the incident laser radiation and its reflection by the substrate and F is the intensity of the diffuse component originated from (multiple) scattering of the collimated components. The substitution of Eq. (6) into RTE (1) and boundary conditions (4) and (5) gives a separate problem for the collimated components [17]

$$\frac{dQ_+}{dz} = -\beta Q_+, \quad \frac{dQ_-}{dz} = \beta Q_-, \quad Q_+(0) = Q_0, \quad Q_-(L) = \rho Q_+(L) \quad (7)$$

with the solution

$$Q_+ = Q_0 e^{-\xi} \text{ and } Q_- = \rho Q_0 e^{\xi-2\lambda} \quad (8)$$

where $\xi = \beta z$ is the dimensionless coordinate and $\lambda = \beta L$ is the optical thickness, as well as the boundary problem for the RTE describing the diffuse radiation [17]

$$\mu \frac{\partial F(z, \mu)}{\partial z} = \frac{\beta \omega}{4\pi} \{Q_+(z)P(1, \mu) + Q_-(z)P(-1, \mu)\} + \beta \left\{ \frac{\omega}{2} \int_{-1}^1 F(z, \mu') P(\mu', \mu) d\mu' - F(z, \mu) \right\} \quad (9)$$

$$F(0, \mu) = 0 \text{ at } \mu > 0 \text{ and } F(L, \mu) = \rho F(L, -\mu) \text{ at } \mu < 0 \quad (10)$$

In the framework of the two-flux method, an approximate solution of Eqs. (9) and (10) is looking for

$$F(z, \mu) = F_+(z)h(\mu) + F_-(z)[1 - h(\mu)] \quad (11)$$

where h is the step Heaviside function. The substitution of Eq. (11) into Eq. (9) and integration over intervals $0 < \mu < 1$ and $-1 < \mu < 0$ gives two moment equations for dimensionless coefficients $f_{\pm} = 2\pi F_{\pm} / Q_0$ [17] as

$$\pm \frac{1}{2} \frac{df_{\pm}}{d\xi} = \frac{\rho}{2} (q_+ + q_- + f_+ + f_-) - f_{\pm} \quad (12)$$

where dimensionless functions $q_+ Q_+ / Q_0 = e^{-\xi}$ and $q_- = Q_- / Q_0 = \rho e^{\xi-2\lambda}$ are introduced and relations (2) and (3) are taken into account. Boundary conditions for f_{\pm} follow from Eq. (10) as

$$f_+(0) = 0 \text{ and } f_-(\lambda) = \rho f_+(\lambda) \quad (13)$$

The general solution of Eq. (12) is

$$f_+ + f_- = C_1 e^{-2a\xi} + C_2 e^{2a\xi} - \frac{4\rho(e^{-\xi} + \rho e^{\xi-2\lambda})}{4\rho - 3} \quad (14)$$

$$f_+ - f_- = aC_1 e^{-2a\xi} - aC_2 e^{2a\xi} - \frac{2\rho(e^{-\xi} - \rho e^{\xi-2\lambda})}{4\rho - 3} \quad (15)$$

where $a = \sqrt{1 - \rho}$. Arbitrary constants C_1 and C_2 are found from boundary conditions (13)

$$C_1 = 2\rho \frac{(1-a)(1-\rho^2)e^{-\lambda} - [1+a-\rho(1-a)]e^{2a\lambda}(3+\rho e^{-2\lambda})}{(4\rho-3)D} \quad (16)$$

$$C_2 = 2\rho \frac{[1-a-\rho(1+a)]e^{-2a\lambda}(3+\rho e^{-2\lambda}) - (1+a)(1-\rho^2)e^{-\lambda}}{(4\rho-3)D} \quad (17)$$

$$D = (1-a)[1-a-\rho(1+a)]e^{-2a\lambda} - (1+a)[1+a-\rho(1-a)]e^{2a\lambda} \quad (18)$$

Net radiative energy flux density is calculated by definition in Ref. [16] as

$$Q = 2\pi \int_{-1}^1 I \mu d\mu = \pi(F_+ - F_-) + Q_+ - Q_- \quad (19)$$

where Eqs. (6) and (11) are taken into account in the right hand side. In the dimensionless form

$$q = \frac{Q}{Q_0} = \frac{f_+ - f_-}{2} + q_+ - q_- = \frac{\rho a}{(4\rho-3)D} \{ (1-\rho^2)e^{-\lambda} [(1-a)e^{-2a\xi} + (1+a)e^{2a\xi}] - (3+\rho e^{-2\lambda}) \times \{ [1+a-\rho(1-a)]e^{2a(\lambda-\xi)} + [1-a-\rho(1+a)]e^{2a(\xi-\lambda)} \} \} - \frac{3(1-\rho)(e^{-\xi} - \rho e^{\xi-2\lambda})}{4\rho-3} \quad (20)$$

Absorptivity of the system powder-substrate defined as the fraction of the incident radiation passed the powder surface, is estimated as

$$A = q(0) = \frac{\rho a}{(4\rho-3)D} \{ 2(1-\rho^2)e^{-\lambda} - (3+\rho e^{-2\lambda}) \times \{ [1+a-\rho(1-a)]e^{2a\lambda} + [1-a-\rho(1+a)]e^{-2a\lambda} \} \} - \frac{3(1-\rho)(1-\rho e^{-2\lambda})}{4\rho-3} \quad (21)$$

The fraction of incident radiation absorbed by the substrate is

$$A_s = q(\lambda) = \frac{\rho a}{(4\rho-3)D} \{ (1-\rho^2)e^{-\lambda} [(1-a)e^{-2a\lambda} + (1+a)e^{2a\lambda}] - 2(1-\rho)(3+\rho e^{-2\lambda}) \} - \frac{3(1-\rho)^2 e^{-\lambda}}{4\rho-3} \quad (22)$$

The volumetric heat source due to radiation absorption is

$$U = -\frac{dQ}{dz} = -\beta Q_0 \frac{dq}{d\xi} \quad (23)$$

3 Conductive Heat Transfer

In the moving coordinate system shown in Fig. 1(c), the heat conduction equation is

$$\frac{\partial H}{\partial t} - v \frac{\partial H}{\partial x} = \frac{\partial}{\partial x} \left(k \frac{\partial T}{\partial x} \right) + \frac{\partial}{\partial y} \left(k \frac{\partial T}{\partial y} \right) + \frac{\partial}{\partial z} \left(k \frac{\partial T}{\partial z} \right) + U \quad (24)$$

where volumetric enthalpy H is related with temperature T by the thermal equation of state

$$T = \begin{cases} H/C_s, & H \leq C_s T_m \\ T_m, & C_s T_m < H < C_s T_m + H_m \\ T_m + (H - C_s T_m - H_m)/C_l, & H \geq C_s T_m + H_m \end{cases} \quad (25)$$

where C_s and C_l are the specific heats in solid and liquid phases, respectively, T_m is the melting point, H_m is the latent heat of melting, t is the time, v is the scanning velocity, k is the thermal conductivity, and U is the volumetric heat source given by Eq. (23). The power density in the laser beam of full radius R is approximated by a bell-like radial distribution

$$Q_0 = Q_m \left(1 - \frac{r}{R} \right)^2 \left(a + \frac{r}{R} \right)^2, \quad 0 < r < R \quad (26)$$

with $r^2 = x^2 + y^2$ and maximum Q_m related to total laser power

$$W = 2\pi \int_0^R Q_0(r) r dr = \frac{\pi}{3} R^2 Q_m \quad (27)$$

Thermal conductivity of metallic powder k_p is about 100 times less than that of dense material k_d [14]. To take into account this difference, phase function ϕ is introduced, which is equal to 0 in the powder phase and 1 in the dense phase. The thermal conductivity is specified as

$$k = k_p + (k_d - k_p) \phi \quad (28)$$

The phase function is initially set to 0 in the powder layer and 1 in the substrate. It is also set to 1 if the temperature T exceeds the melting point T_m , which means consolidation of powder. Outside the melting zone, the evolution of the phase function is calculated from the transport equation

$$\frac{\partial \phi}{\partial t} - v \frac{\partial \phi}{\partial x} = 0 \quad (29)$$

Equation (29) applied outside the melting front is independent of heat transfer equation (24). The phase function ϕ depends on temperature through its boundary condition at the melting front, where ϕ is assigned the value of 1. This equation is introduced to trace the points of powder where the temperature has ever been above the melting temperature, and therefore the matter tends to change from the dispersed state to the dense state.

Equations (24) and (29) are numerically solved in the rectangular computation domain $\{x = -X^-, \dots, X^+; y = 0, \dots, Y; z = 0, \dots, Z\}$ with faces $x = -X^-$, $x = X^+$, $y = Y$, and $z = Z$ far from the origin not to influence the laser-matter interaction zone. The boundary conditions of isolated walls are used at the faces of the domain for Eq. (24)

$$\frac{\partial H}{\partial \mathbf{n}} = 0 \quad (30)$$

where \mathbf{n} is the normal to the corresponding face. This condition also assures the mirror symmetry against plane $y=0$. Equation (29) requires a boundary condition at face $x = -X^-$ as

$$\phi = \begin{cases} 0, & z < L \\ 1, & z \geq L \end{cases} \quad (31)$$

where L is the thickness of the powder layer, and a boundary condition at the melting front

$$\phi = 1 \quad (32)$$

which is applied in the three-dimensional domain where $T \geq T_m$ in the numerical procedure but changes nothing downstream the melting front.

The computational domain is divided into $N_x \times N_y \times N_z$ rectangular cells with the sizes of $\Delta x = (X^- + X^+)/N_x$, $\Delta y = Y/N_y$, and $\Delta z = Z/N_z$ and the centers at $x_i = -X^- + \Delta x/2 + i\Delta x$, $y_j = \Delta y/2 + j\Delta y$, and $z_l = \Delta z/2 + l\Delta z$, with integers $i = 0, \dots, N_x - 1$, $j = 0, \dots, N_y - 1$, and $l = 0, \dots, N_z - 1$. The typical parameters are $N_x \times N_y \times N_z = 240 \times 80 \times 80$ and $\Delta x = \Delta y = \Delta z = 2.5 \mu\text{m}$. The convergence of the numerical scheme was checked by calculating the same problem at the grid with the number of cells reduced by a factor of 2 in each dimension, and no significant differences in results were obtained.

The heat transfer equation (24) is approximated by the following explicit conservative finite-difference scheme with second order accuracy in space and first order accuracy in time

$$\begin{aligned} & \frac{H_{ijl}(t + \Delta t) - H_{ijl}(t)}{\Delta t} - v \frac{H_{i+1/2,jl}(t) - H_{i-1/2,jl}(t)}{\Delta x} \\ &= \frac{1}{\Delta x} \left[\frac{k(T_{i+1,jl}) + k(T_{ijl})}{2} \frac{T_{i+1,jl}(t) - T_{ijl}(t)}{\Delta x} \right. \\ & \quad \left. - \frac{k(T_{ijl}) + k(T_{i-1,jl})}{2} \frac{T_{ijl}(t) - T_{i-1,jl}(t)}{\Delta x} \right] \\ & \quad + \frac{1}{\Delta y} \left[\frac{k(T_{i,j+1,l}) + k(T_{ijl})}{2} \frac{T_{i,j+1,l}(t) - T_{ijl}(t)}{\Delta y} \right. \\ & \quad \left. - \frac{k(T_{ijl}) + k(T_{i,j-1,l})}{2} \frac{T_{ijl}(t) - T_{i,j-1,l}(t)}{\Delta y} \right] \\ & \quad + \frac{1}{\Delta z} \left[\frac{k(T_{ij,l+1}) + k(T_{ijl})}{2} \frac{T_{ij,l+1}(t) - T_{ijl}(t)}{\Delta z} \right. \\ & \quad \left. - \frac{k(T_{ijl}) + k(T_{ij,l-1})}{2} \frac{T_{ijl}(t) - T_{ij,l-1}(t)}{\Delta z} \right] \end{aligned} \quad (33)$$

where Δt is the time increment, the grid function H_{ijl} is defined as the cell average, and T_{ijl} is calculated by the thermal equation of state (25). The advection equation (29) is approximated as

$$\frac{\phi_{ijl}(t + \Delta t) - \phi_{ijl}(t)}{\Delta t} = v \frac{\phi_{i+1/2,jl}(t) - \phi_{i-1/2,jl}(t)}{\Delta x} \quad (34)$$

The grid functions H_{ijl} and ϕ_{ijl} are defined as the cell averages, T_{ijl} is calculated by the thermal equation of state (25), and the half-integer values $H_{i+1/2,jl}$ and $\phi_{i+1/2,jl}$ are estimated from the corresponding integer values by the "minmod" slope limiter method [18] to obtain a nonoscillatory second order approximation of the advection terms.

The time step Δt is restricted by the stability conditions for the explicit schemes

$$\Delta t < \frac{\Delta x^2}{8a}, \quad \Delta t < v \Delta x \quad (35)$$

where Δx is the minimum cell size and a the maximum thermal diffusivity. The typical value of Δt is of the order of 10^{-7} s.

4 Thermal and Optical Properties

Calculations are made for stainless steel type 316L with a melting point $T_m = 1700$ K, a latent heat of melting $H_m = 2.18$ GJ/m³, and specific heats of $C_s = 4.25$ MJ/m³ K in solid and $C_l = 5.95$ MJ/m³ K in liquid phases. Thermal conductivity of this alloy considerably increases with temperature above the room temperature. The temperature range near the melting point and above is the most important for the studied problem where there

are no reliable experimental data, so that a constant value of $k_d = 20 \text{ W/m K}$ is accepted, which is obtained by extrapolation to the melting point.

The effective thermal conductivity of loose metallic powders is controlled by gas in the pores [14]. Therefore, it is essentially independent of material but depends on the size and morphology of the particles and the void fraction, as well as on the thermal conductivity of the gas. For $10\text{--}50 \text{ }\mu\text{m}$ powders, the effective thermal conductivity is typically from 0.1 to 0.2 W/m K in air at room temperature [14]. The thermal conductivity of gas increases approximately as square root of temperature, so that a value around $k_p = 0.3 \text{ W/m K}$ is expected near the melting point. This value is still much less than the thermal conductivity of solid, so that the modeling results are not expected to be sensitive to the thermal conductivity of powder. The above constant value at the melting point is used in calculations. The thermal dependence is neglected. The contribution of radiative heat transfer to the thermal conductivity k_r can be estimated as [19]

$$k_r = \frac{16l}{3} \sigma T^3 \quad (36)$$

where l is Rosseland's path and σ is the Stephan–Boltzmann constant. The value of l is around the grain size in the powder bed. The typical values of $l = 20 \text{ }\mu\text{m}$ and $T = 2000 \text{ K}$ result in $k_r = 0.05 \text{ W/m K}$. This is much less than k_p , and so the radiative heat transfer is neglected in the model.

The optical properties are estimated for the laser wavelength of $1.075 \text{ }\mu\text{m}$. The hemispherical reflectivity of pure iron $\rho = 0.7$ is accepted for steel 316L. This is consistent with experimental data for powders of this steel [17,20] obtained at the room temperature. The temperature dependence is neglected because of lack of data. The extinction coefficient β of loose powders was measured in Ref. [21], where a strong dependence on the size and the morphology of particles was reported. It can be estimated by Eq. (2). Assuming that the powder bed consists of spherical particles of diameter D distributed in space with number density n , this equation gives

$$\beta = \frac{1}{4} \frac{\pi D^2 n}{1 - \pi D^3 n/6} = \frac{3}{2} \frac{1 - \varepsilon}{\varepsilon} \frac{1}{D} \quad (37)$$

where porosity $\varepsilon = 1 - \pi D^3 n/6$ is defined. The optical thickness

$$\lambda = \beta L = \frac{3}{2} \frac{1 - \varepsilon}{\varepsilon} \frac{L}{D} \quad (38)$$

is proportional to the number of monolayers (L/D). For typical parameters of $D = 20 \text{ }\mu\text{m}$ and $L = 50 \text{ }\mu\text{m}$ ($L/D = 2.5$ monolayers), the optical thickness is estimated as $\lambda = 3.75$ for porosity $\varepsilon = 1/2$ and $\lambda = 1.875$ for $\varepsilon = 2/3$.

5 Estimation of Laser Energy Deposition

Figure 3 shows the depth profiles of radiative energy flux and volumetric heat source in the powder layer calculated by Eqs. (20) and (23), respectively. Vertical line on the right of each curve corresponds to the substrate surface. Approximately linear decrease in the flux at low optical thickness ($\lambda = 1$ in Fig. 3(a)) evolves into approximately exponential decay with increasing the optical thickness ($\lambda = 4$ in Fig. 3(a)). The corresponding energy deposition distributions (Fig. 3(b)) are proportional to the derivative of the flux. They change from a roughly uniform distribution over the powder layer at $\lambda = 1$ to an approximately exponential function at $\lambda = 4$. The deviation from the exponential Beer–Lambert–Bouguer law is due to the radiation scattering in the powder.

The fraction of incident laser radiation absorbed by the substrate A_s decreases with the optical thickness of the powder layer (lower curve in Fig. 4, calculated by Eq. (22)), while the fraction absorbed in the powder $A - A_s$ increases (middle curve) so that the

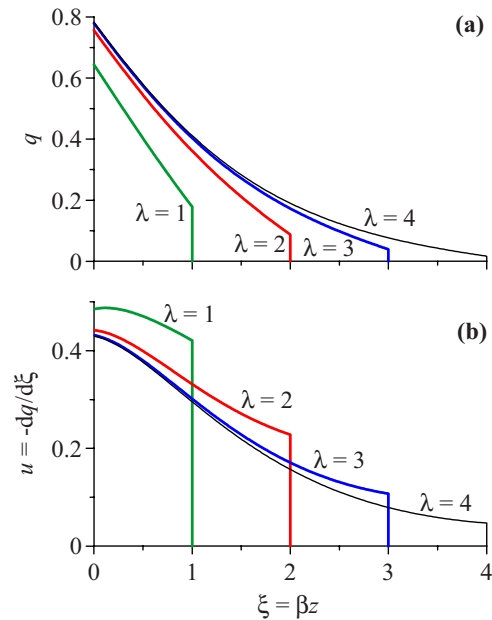


Fig. 3 (a) Dimensionless radiative flux $q = Q/Q_0$ and (b) volumetric heat source $u = U/(\beta Q_0)$ in the powder layer versus dimensionless depth ξ for various values of optical depth λ at the reflectivity of dense material $\rho = 0.7$

total absorptivity A considerably increases (upper curve, calculated by Eq. (21)) relative to the absorptivity of dense material $1 - \rho = 0.3$.

Figure 5 shows the radial profiles of power density Q_0 in the incident laser beam, which are employed for the calculations. They are specified according to Eqs. (26) and (27) by total beam

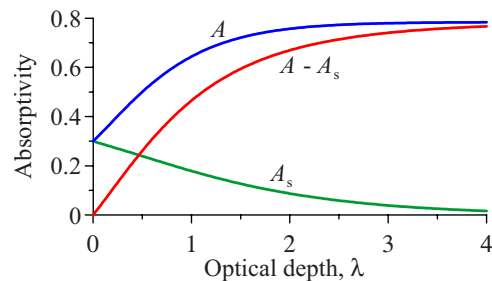


Fig. 4 Total absorptivity of the system powder-substrate A and fractions of the incident laser radiation absorbed by the surface of the substrate A_s and in the powder $A - A_s$ versus optical depth of the powder layer λ at the reflectivity of dense material $\rho = 0.7$

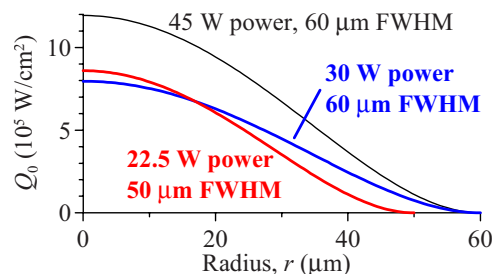


Fig. 5 Radial profiles of power density in the incident laser beam employed for the calculations. The total beam power and the FWHM are specified for each curve.

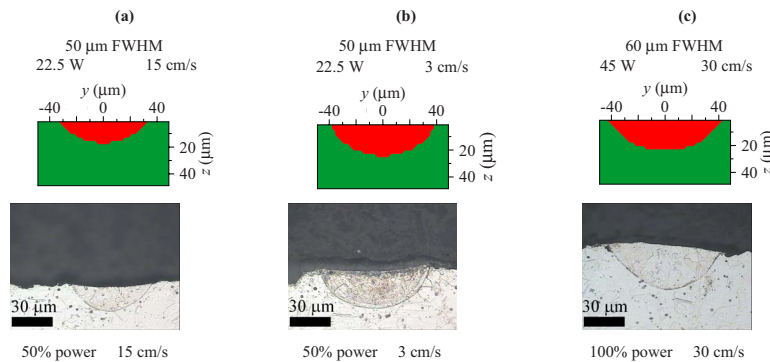


Fig. 6 Cross-sections of laser tracks on the stainless steel substrate without powder: calculated phase diagrams (upper row) and experimental micrographs (lower row)

power W and full radius R , which is approximately equal to the full width of the beam at half maximum (FWHM).

6 Results and Discussion

The experimental results are obtained with SLM machine “Phenix Systems” employing $1.075 \mu\text{m}$ laser of 50 W nominal power and $70 \mu\text{m}$ nominal beam diameter. Taking into account absorption by the optical system, the maximum laser power is estimated as 45 W. The pumping power of the laser can be reduced producing laser radiation of reduced power, which is measured in fractions of the maximum power.

To validate the model, heat transfer in the substrate without powder is modeled first. Figure 6 compares experimental cross section micrographs (on the bottom) with the calculated projections of the melt pool on the plane perpendicular to the scanning direction (on the top). The absorbed fraction of laser energy $1 - \rho = 0.3$ used in calculations is expected to be the most uncertain model parameter because it is estimated from the reflectivity ρ measured at the room temperature, while the absorptivity of metals generally tends to increase with temperature. Another questionable point of the model is the negligence of the Marangoni convection in the melt pool. Both the increase in absorptivity with temperature and the convection enlarge the melt pool. The ob-

served agreement between the experiment and the model shown in Fig. 6 indicates that the absorptivity does not significantly increase with temperature and the contribution of the Marangoni convection to heat transfer is low.

The diameter of the laser beam is evaluated by its traces at reduced laser power. The full diameter estimated from such experiments is around $100 \mu\text{m}$. However, a slow dependence on the laser power is possible. Therefore, two values of FWHM diameter of $50 \mu\text{m}$ and $60 \mu\text{m}$ were tested in the calculations. The difference was not principal. However, the shape of the experimental melt pool is reproduced better by $50 \mu\text{m}$ FWHM at 50% power (22.5 W) and by $60 \mu\text{m}$ FWHM at 100% power (45 W).

Figure 7 presents the typical modeling results for a $50 \mu\text{m}$ powder layer on a substrate. The isotherms in diagrams (c) and (d) show the melting point $T_m = 1700 \text{ K}$. The level in diagram (e) is the powder-substrate interface. The incident laser power of 30 W chosen for this calculation is less than the maximum of 45 W to take into account heat losses by evaporation. According to the preliminary calculations, the beam of 45 W incident power considerably overheats the powder layer above the boiling point because of low thermal conductivity of powder. Indeed, while no evaporation is experimentally observed from the noncovered substrate, the traces of evaporation as ejection of droplets are noticed

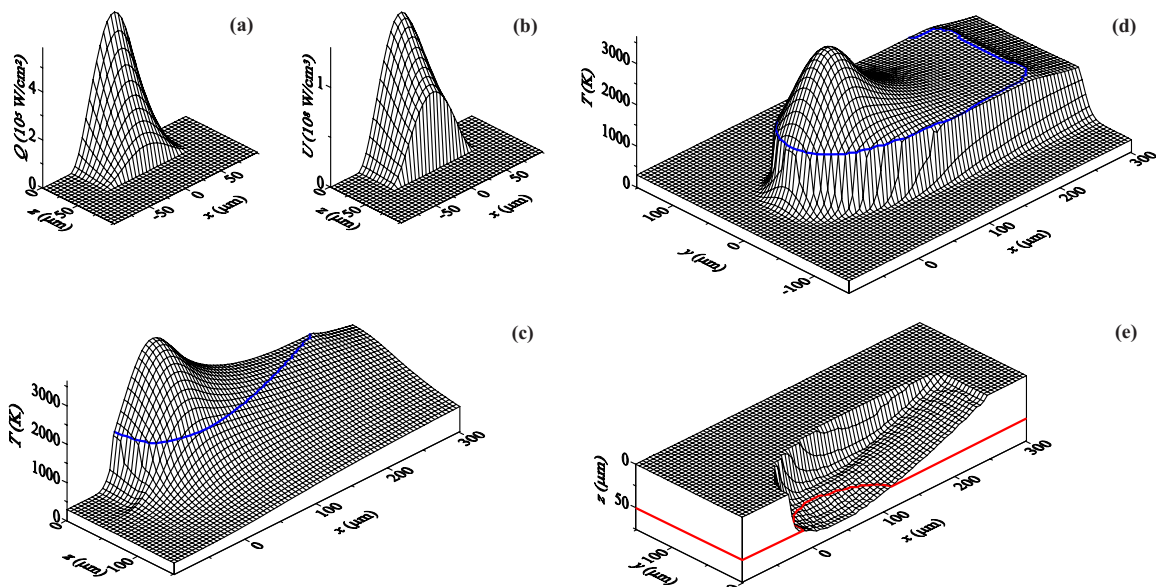


Fig. 7 Laser beam scanning of a $50 \mu\text{m}$ powder layer with optical thickness $\lambda=2$ at the incident laser power of 30 W, the laser beam FWHM of $60 \mu\text{m}$, and the scanning velocity of 20 cm/s. Distributions at the symmetry plane $y=0$: (a) normal component of net laser radiation flux density Q , (b) volumetric heat source due to absorption of laser radiation U , (c) temperature T , (d) temperature T at the top powder surface $z=0$, and (e) melt pool shape.

for the sandwich powder/substrate [3]. The fraction of the evaporated material is experimentally estimated to be low. Nevertheless, the evaporation can contribute to the energy balance of the process.

Two principal effects of evaporation are expected. First, the hot vapor and the droplets shield the target from the incident laser radiation so that the beam intensity at the target surface is reduced. Second, the thermal energy released after the laser beam absorption is partly spent to evaporation and taken away with vapor. These complex processes are taken into account by reducing the incident laser power. The value of 30 W is found to result in reasonable maximum temperatures around the boiling point. The same effective incident laser power of 30 W is applied to all the calculations made for the powder/substrate system.

The net laser energy flux density Q (Fig. 7(a)) and volumetric heat source U (Fig. 7(b)) are estimated by Eqs. (20), (23), and (26). The value of Q at the top powder surface $z=0$ gives total power density absorbed by the system powder layer substrate. It is less than the corresponding incident power density given by the blue curve in Fig. 5. The value of Q at the powder-substrate interface $z=50\text{ }\mu\text{m}$ gives power density absorbed by the surface of the substrate, which is considerably less than the incident one. The volumetric deposition of laser energy decreases with the depth according to Fig. 7(b) but is important until the bottom of the powder layer.

The influence of the scanning velocity v on conductive heat transfer is estimated by the Peclet number $Pe=vR/\chi$ with thermal diffusivity χ . The thermal diffusivity of the dense solid phase is estimated as $4.7\text{ mm}^2/\text{s}$ from the parameters listed in Sec. 4, while the value of $0.07\text{ mm}^2/\text{s}$ is obtained for the powder. For the example shown in Fig. 7, these two different diffusivities give the Peclet number of ~ 2.6 in the dense material and ~ 170 in the powder. In the center of the melt pool, where the Peclet number is about unity, the influence of the scanning is small and the temperature distribution is approximately symmetric about axis (OZ) because the laser beam is axially symmetric. However, the temperature maximum is slightly shifted relative at the center of the laser beam. This is clearer in Fig. 8(d), where the projection of the laser beam on the surface is shown by a broken-line circle. At the periphery of the melt pool and especially near the powder phase, the Peclet number is large, so that the scanning considerably violates the axial symmetry. Therefore, the melt pool is highly stretched along the scanning direction (see Fig. 7(e)).

The sharp edge in the temperature distribution of Fig. 7(d) at the powder-liquid boundary (front boundary of the melt pool) appears due to a high difference in thermal conductivity. The similar edge at the rear boundary of the melt pool is due to liberation of the latent heat at solidification.

Figure 8 presents the experimental top view of the remelted tracks (a) and their cross section micrographs (b), as well as the calculated temperature distribution on the top powder surface (d) and phase distribution in the cross-section (c) at various scanning velocities. The zones of the remelted material (center), loose powder (top sides), and the substrate (bottom) are distinguished by contrast in Fig. 8(c). The experiments are made at the incident laser power of $\sim 45\text{ W}$ and $\sim 60\text{ }\mu\text{m}$ FWHM. To take into account heat losses by evaporation, the reduced effective laser power of 30 W is used for the calculations as explained above. The thickness of the powder layer is fixed to $L=50\text{ }\mu\text{m}$. However, its optical thickness λ depends on the porosity, which is not controlled in the experiments. Therefore, calculations are made at two values of $\lambda=2$ and 3.

The maximum surface temperature (see Fig. 8(d)) considerably exceeds the boiling point of $\sim 3200\text{ K}$, especially at lower scanning velocity. This is consistent with the experimentally observed intensive evaporation. The maximum temperature could be less if the radiative thermal conductivity proportional to T^3 according to Eq. (29) were taken into account. The volumetric heat source U in Eq. (24) is evaluated by the one-dimensional radiation transfer

model. Application of this model for the present problem where the laser beam width ($60\text{ }\mu\text{m}$) is comparable with the characteristic depth ($50\text{ }\mu\text{m}$) overestimates U in the center, so that the temperature maximum is expected to be overestimated too. The boiling point isotherm at $T=1700\text{ K}$ (bold curves in Fig. 8(d)) gives the top contour of the melt pool. The melt pool becomes longer and narrower with increasing the scanning velocity. Its top surface slightly increases with the optical thickness λ because of redistribution of the heat source U , more energy is deposited near the surface.

The calculated shape of the remelted zone (Fig. 8(c)) is quite different from the experimentally observed one (Fig. 8(b)) and indicates melt flow not taken into account by the model. This flow is expected to be driven by the surface tension force. Indeed, the initially molten powder is attached to the substrate in the central part of the melt pool, while its lateral parts do not contact with the substrate (see Fig. 8(c)). Therefore, the sides completely detach from the substrate and the nonmelted powder to form a rounded free surface, as shown in Fig. 8(b), which reduces the surface energy. The melt deformation is schematically shown in Fig. 9. This mechanism explains the bright zones at the sides of the remelted cylinders on the top view (a), which are interpreted as the substrate surface became visible because the powder above it is consumed. Comparison between Figs. 8(a) and 8(d) indicates that the width of the powder-consumed band approximately corresponds to the calculated maximum width of the melt pool. This suggests that the melt flow is weak in the forward half of the pool ($x < 100\text{ }\mu\text{m}$), so that the heat transfer model gives the correct value of its maximum width. On the contrary, a strong melt flow is expected in the backward half ($x > 100\text{ }\mu\text{m}$), where the results given by the model are rough.

The surface tension-driven flow is supposed to be negligible in the central bottom part of the melt pool, so that the shape of the remelted zone of the substrate is correctly estimated by the model (compare Figs. 8(b) and 8(c)). In particular, the width of the contact between the remelted powder and the substrate is quite correct. This is confirmed by Fig. 10, where the two characteristic dimensions of the remelted track are plotted as functions of the scanning velocity. The calculated width of the powder-consumed band is defined as the maximum width of the melt pool and taken from Figs. 8(c) and 8(d). The calculated width of the contact is defined as the maximum width of the melt pool at the substrate surface ($z=50\text{ }\mu\text{m}$) and taken from Fig. 8(c). The corresponding experimental values are taken from Figs. 8(a) and 8(b). Comparison between calculations for $\lambda=2$ and $\lambda=3$ indicates that these two dimensions are not sensitive to the optical thickness λ . Both the width of the powder-consumed band and the width of the contact decrease with the scanning velocity v , as shown in Fig. 10. Experimental contact width becomes noisy above $v=14\text{ cm/s}$. At such high scanning velocities, the process becomes unstable, and the remelted cylinder tends to break into separate droplets (see Fig. 8(a) for $v=20$ and 24 cm/s). For example, the cross section micrograph shown in Fig. 8(b) for $v=20\text{ cm/s}$ is likely to pass across such a droplet. Therefore, the remelted zone is considerably larger than in the neighbor micrographs. The width of the contact with the substrate considerably varies along the track at high v . This produces the experimental uncertainty and the discrepancy with the calculations shown in Fig. 10.

Fragmentation of the remelted tracks at SLM is a well-known drawback of the technique referred to as the "balling" effect [22]. An interval of the scanning velocity where the SLM process is stable was shown to exist for the conditions similar to those tested in this work [3,23]. The "balling" effect appears both at the lower and the upper bounds of this interval. It is explained by a capillary instability of the melt pool at high length-to-width ratios when it fragments with reducing the surface energy [23]. The fragmentation shown on the right of Fig. 8(a) concerns the upper stability limit at $v \sim 20\text{ cm/s}$. According to the micrographs in Fig. 8(b),

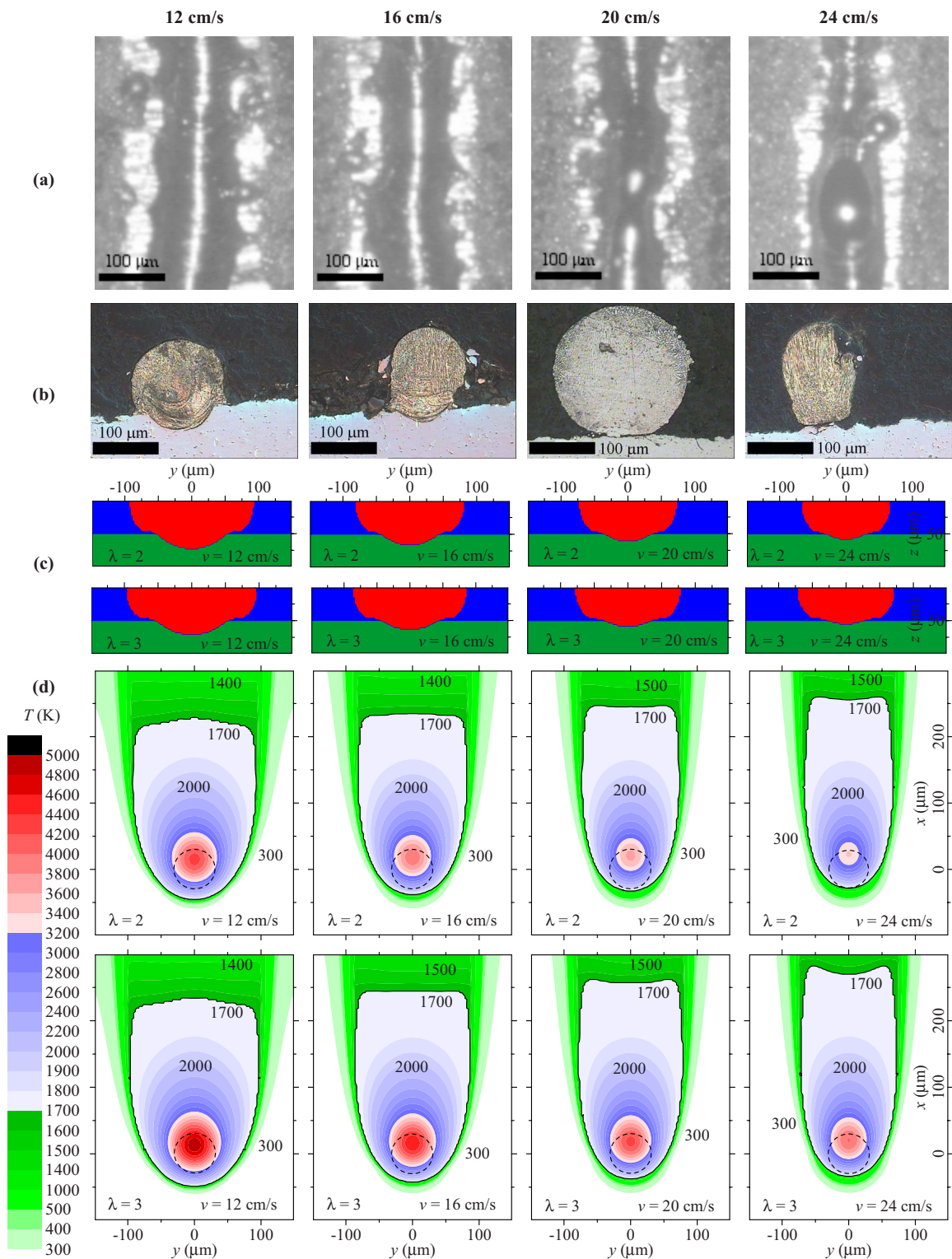


Fig. 8 Comparison between experiments ((a) and (b)) and calculations ((c) and (d)) at various scanning velocities (marked on the top of each column): (a) top view of remelted tracks; (b) cross section micrographs; (c) calculated phase distribution in cross-section with the substrate on the bottom, the powder on the sides, and the remelted zone in the center; and (d) surface temperature distribution. The broken-line circles on diagrams (d) are projections of the laser beam.

the contact between the remelted powder and the substrate tends to vanish at $v > 20$ cm/s. While the calculated contact width at this velocity is still about $60\ \mu\text{m}$, the modeling indicates that this parameter is the most sensitive to v and decreases fast. Therefore,

the upper stability limit can also be related to the loss of the contact between the molten powder and the substrate.

As shown in Fig. 8(d), the length of the melt pool at the stability limit $v=20$ cm/s is about $300\ \mu\text{m}$ and its width about

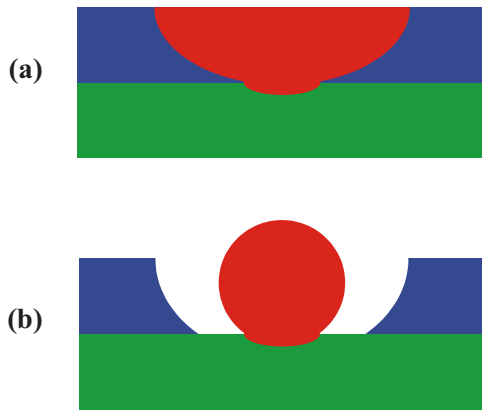


Fig. 9 Qualitative evolution of phase distribution in the cross-section of a track with the substrate on the bottom, the powder on the sides, and the melt in the center: (a) just melted and (b) after minimizing the melt surface

150 μm . The height is equal to the powder layer thickness $L = 50 \mu\text{m}$. According to the above discussion, the surface tension transforms this liquid volume to a shape similar to a circular cylinder with the length of 300 μm and the diameter about 100 μm estimated from volume conservation. The circumference of this cylinder is about its length, which is the limit of the Plateau-Rayleigh capillary instability of a liquid cylinder [24]: The cylinder breaks into two droplets if the length exceeds the circumference. The ratio of the length to the circumference would be greater than unity if the radial shrinkage due to gas ejection from pores were taken into account. Thus, the Plateau-Rayleigh instability can explain the balling effect at $v=20 \text{ cm/s}$. When the scanning velocity v decreases, the length of the melt pool decreases and its width increases (see Fig. 8(d)), so that the Rayleigh ratio of length-to-circumference decreases, which should stabilize the melt pool. However, the crucial stabilizing factor could be the contact between the melt cylinder and the substrate, which disappears at $v \sim 20 \text{ cm/s}$ and increases fast with decreasing the velocity. To break into droplets, the melt should be detached from the substrate between the droplets, which creates additional free surface. This explains the stabilizing effect of the contact.

7 Conclusion

The proposed model of laser beam interaction with the powder bed at SLM consists in coupled radiation and heat transfer in a thin powder layer deposited on a dense substrate. At the studied

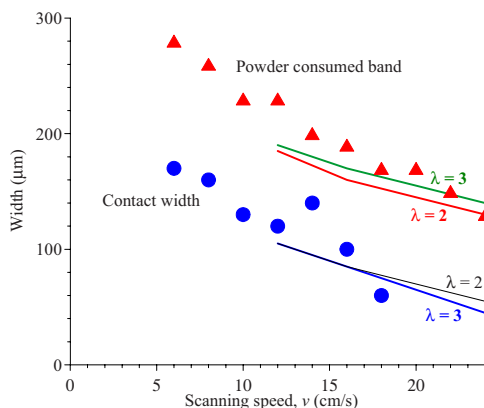


Fig. 10 Widths of the powder-consumed band and the contact of the remelted material with the substrate versus the scanning velocity: experiments (points) and calculations (lines) at two values of the optical thickness, $\lambda=2$ and $\lambda=3$

layer thickness of $\sim 50 \mu\text{m}$ and grain size of $\sim 20 \mu\text{m}$, laser radiation can penetrate into powder by an open pore system until the substrate and create a volumetric heat source. The melt pool formed around the laser beam contacts the substrate by its central part only. Such a complex shape of the melt surface can produce its deformation driven by surface tension. The lateral parts of the melt pool are expected to detach from the neighbor powder to form a rounded free surface with reduced surface energy. Thus, a cylinderlike remelted volume attached to the substrate is formed in the middle of a considerably larger powder-consumed band. The widths of the powder-consumed band and the contact between the remelted material and the substrate can be estimated by the thermal model neglecting melt flow. The balling effect at high scanning velocities (above $\sim 20 \text{ cm/s}$ for the present conditions) can be explained by the Plateau-Rayleigh capillary instability of a liquid cylinder. Two factors destabilize the process with increasing the scanning velocity: increasing the length-to-circumference ratio and decreasing the width of the contact with the substrate. The modeling results can be used to predict whether the balling effect is expected.

Acknowledgment

The authors would like to thank Direction Générale des Entreprises, Conseil Général de la Loire, and Saint-Etienne Métropole for their financial support of the "MULTIMAT" Project, within the Competitiveness Cluster ViaMéca, and also to CETIM Foundation for its financial support of the "Multimatériau and Multifunctional Products" Project.

References

- [1] Santos, E. C., Shiomi, M., Osakada, K., and Laoui, T., 2006, "Rapid Manufacturing of Metal Components by Laser Forming," *Int. J. Mach. Tools Manuf.*, **46**, pp. 1459–1468.
- [2] Yadroitsev, I., Bertrand, Ph., Laget, B., and Smurov, I., 2007, "Application of Laser Assisted Technologies for Fabrication of Functionally Graded Coatings and Objects for the International Thermonuclear Experimental Reactor Components," *J. Nucl. Mater.*, **362**, pp. 189–196.
- [3] Yadroitsev, I., Bertrand, Ph., and Smurov, I., 2007, "Parametric Analysis of the Selective Laser Melting Process," *Appl. Surf. Sci.*, **253**, pp. 8064–8069.
- [4] Choi, J., Han, L., and Hua, Y., 2005, "Modeling and Experiments of Laser Cladding With Droplet Injection," *ASME J. Heat Transfer*, **127**, pp. 978–986.
- [5] Bugada, G., Cervera, M., and Lombra, G., 1999, "Numerical Prediction of Temperature and Density Distributions in Selective Laser Sintering Processes," *Rapid Prototyping J.*, **5**, pp. 21–26.
- [6] Tontowi, A. E., and Childs, T. H. C., 2001, "Density Prediction of Crystalline Polymer Sintered Parts at Various Powder Bed Temperatures," *Rapid Prototyping J.*, **7**, pp. 180–184.
- [7] Tolochko, N. K., Arshinov, M. K., Gusarov, A. V., Titov, V. I., Laoui, T., and Froyen, L., 2003, "Mechanisms of Selective Laser Sintering and Heat Transfer in Ti powder," *Rapid Prototyping J.*, **9**, pp. 314–326.
- [8] Xiao, B., and Zhang, Y., 2008, "Numerical Simulation of Direct Metal Laser Sintering of Single-Component Powder on Top of Sintered Layers," *ASME J. Manuf. Sci. Eng.*, **130**, p. 041002.
- [9] Matsumoto, M., Shiomi, M., Osakada, K., and Abe, F., 2002, "Finite Element Analysis of Single Layer Forming on Metallic Powder Bed in Rapid Prototyping by Selective Laser Processing," *Int. J. Mach. Tools Manuf.*, **42**, pp. 61–67.
- [10] Patil, R. B., and Yadava, V., 2007, "Finite Element Analysis of Temperature Distribution in Single Metallic Powder Layer During Metal Laser Sintering," *Int. J. Mach. Tools Manuf.*, **47**, pp. 1069–1080.
- [11] Kolossov, S., Boillat, E., Gildard, R., Fisher, P., and Locher, M., 2004, "3D FE Simulation for Temperature Evolution in the Selective Laser Sintering Process," *Int. J. Mach. Tools Manuf.*, **44**, pp. 117–123.
- [12] Gusarov, A. V., Yadroitsev, I., Bertrand, Ph., and Smurov, I., 2007, "Heat Transfer Modeling and Stability Analysis of Selective Laser Melting," *Appl. Surf. Sci.*, **254**, pp. 975–979.
- [13] Klocke, F., and Wagner, C., 2003, "Coalescence Behaviour of Two Metallic Particles as Base Mechanism of Selective Laser Sintering," *CIRP Ann.*, **52**, pp. 177–180.
- [14] Rombouts, M., Froyen, L., Gusarov, A. V., Bentefour, E. H., and Glorieux, C., 2005, "Photopyroelectric Measurement of Thermal Conductivity of Metallic Powders," *J. Appl. Phys.*, **97**, p. 024905.
- [15] Wang, X. C., Laoui, T., Bonse, J., Kruth, J. P., Lauwers, B., and Froyen, L., 2002, "Direct Selective Laser Sintering of Hard Metal Powders: Experimental Study and Simulation," *Int. J. Adv. Manuf. Technol.*, **19**, pp. 351–357.
- [16] Siegel, R., and Howell, J. R., 1981, *Thermal Radiation Heat Transfer*, Hemisphere, New York.
- [17] Gusarov, A. V., and Kruth, J.-P., 2005, "Modelling of Radiation Transfer in Metallic Powders at Laser Treatment," *Int. J. Heat Mass Transfer*, **48**, pp.

- [18] Leveque, R. J., 1992, *Numerical Methods for Conservation Laws*, Birkhauser Verlag, Berlin.
- [19] Zel'dovich, Y. B., and Raiser, Y. P., 1967, *Physics of Shock Waves and High-Temperature Hydrodynamic Phenomena*, Academic, New York.
- [20] Gusarov, A. V., Bentefour, E. H., Rombouts, M., Froyen, L., Glorieux, C., and Kruth, J.-P., 2006, "Normal-Directional and Normal-Hemispherical Reflectances of Micron- and Submicron-Sized Powder Beds at 633 and 790 nm," *J. Appl. Phys.*, **99**, p. 113528.
- [21] Rombouts, M., Froyen, L., Gusarov, A. V., Bentefour, E. H., and Glorieux, C., 2005, "Light Extinction in Metallic Powder Beds: Correlation With Powder Structure," *J. Appl. Phys.*, **98**, p. 013533.
- [22] Morgan, R., Sutcliffe, C. J., and O'Neill, W., 2001, "Experimental Investigation of Nanosecond Pulsed Nd:YAG Laser Re-Melted Pre-Placed Powder Beds," *Rapid Prototyping J.*, **7**, pp. 159–172.
- [23] Kruth, J. P., Froyen, L., Van Vaerenbergh, J., Mercelis, P., Rombouts, M., and Lauwers, B., 2004, "Selective Laser Melting of Iron-Based Powder," *J. Mater. Process. Technol.*, **149**, pp. 616–622.
- [24] Chandrasekhar, S., 1961, *Hydrodynamic and Hydromagnetic Stability*, Clarendon, Oxford.